applied optics

Spectral bidirectional texture function reconstruction by fusing multiple-color and spectral images

WEI DONG,[1] HUI-LIANG SHEN,[1,*] XIN DU,[1] SI-JIE SHAO,[2] AND JOHN H. XIN[2]

[1]College of Information Science and Electronic Engineering, Zhejiang University, Hangzhou 310027, China
[2]Institute of Textiles and Clothing, The Hong Kong Polytechnic University, Hong Kong, China
*Corresponding author: shenhl@zju.edu.cn

Received 16 August 2016; revised 27 November 2016; accepted 27 November 2016; posted 29 November 2016 (Doc. ID 273959); published 19 December 2016

Spectral bidirectional texture function (BTF) is essential for accurate reproduction of material appearance due to its nature of conveying both spatial and spectral information. A practical issue is that the acquisition of raw spectral BTFs is time-consuming. To resolve the limitation, this paper proposes a novel framework for efficient spectral BTF acquisition and reconstruction. The framework acquires red-green-blue (RGB) BTF images and just one spectral image. The full spectral BTFs are reconstructed by fusing the RGB and spectral images based on nonnegative matrix factorization (NMF). Experimental results indicate that the accuracy of spectral reflectance reconstruction is higher than that of existing algorithms. With the reconstructed spectral BTFs, the material appearance can be reproduced with high fidelity under various illumination conditions.

OCIS codes: (290.1483) BSDF, BRDF, and BTDF; (110.4234) Multispectral and hyperspectral imaging; (330.1730) Colorimetry; (330.1710) Color, measurement.

https://doi.org/10.1364/AO.55.010400

1. INTRODUCTION

Accurate reproduction of material appearance is required in many industries, including automobile, painting, textile, etc. Hence, there is a need to acquire the exact information about the reflectance properties of a material. The reflectance properties of a homogeneous material under different viewing and lighting directions can be described by the bidirectional reflectance distribution function (BRDF) [1]. The BRDF $f_{\mathrm{brdf}}(\omega_i, \omega_o, \lambda)$ is defined as the ratio of reflected radiance L exiting from a surface in a direction $\omega_o := (\theta_o, \phi_o)$, to the irradiance incident E on the surface from direction $\omega_i := (\theta_i, \phi_i)$, for a particular wavelength λ, as follows:

$$f_{\mathrm{brdf}}(\omega_i, \omega_o, \lambda) = \frac{\mathrm{d}L(\omega_o, \lambda)}{\mathrm{d}E(\omega_i, \lambda)}. \tag{1}$$

The BRDF can be represented as physics-based analytic models such as the Cook–Torrance [2], Ward [3], and He [4] models. These representations make the BRDF convenient to use in practical applications such as computer graphics rendering. Alternatively, the BRDF data can be sampled densely enough from the material of the real world and used directly as a table-based model [5].

Despite its convenient usage, the BRDF is suitable only for homogeneous materials that do not contain textures. In the real world, however, a variety of rough surfaces have complicated spatial structures. These rough surfaces cause various effects such as shadowing, masking, interreflection, and subsurface scattering, which cannot be described by the BRDF. The bidirectional texture function (BTF) was introduced by Dana *et al.* [6] to capture at least some of these effects. As illustrated in Fig. 1, the BTF $f_{\mathrm{btf}}(p, \omega_i, \omega_o, \lambda)$ is a seven-dimensional function of surface position p, lighting direction ω_i, viewing direction ω_o, and wavelength λ, as follows:

$$f_{\mathrm{btf}}(p, \omega_i, \omega_o, \lambda) = \frac{\mathrm{d}L(p, \omega_o, \lambda)}{\mathrm{d}E(p, \omega_i, \lambda)}. \tag{2}$$

The behavior of BTFs is usually too complicated to be synthesized through analytic models or simple simulations. Hence, state-of-the-art methods, known as image-based models, have been developed to represent BTF data [7–9]. These methods rely on measured BTFs (acquired real-world data) in combination with appropriate synthesis methods. Because multispectral imaging cameras are expensive, and the measuring process is time consuming, BTFs are generally captured using

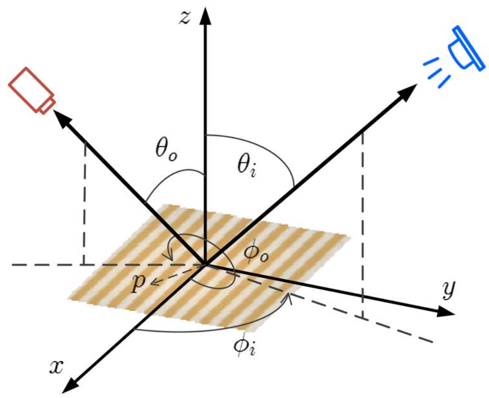

Fig. 1. Parameters describing BTF geometry in the sample coordinate system, including the viewing direction $\omega_o := (\theta_o, \phi_o)$, lighting direction $\omega_i := (\theta_i, \phi_i)$, and pixel position $p := (x, y)$.

RGB cameras [10,11], and the BTF becomes $f_{\mathrm{btf}}(p, \omega_i, \omega_o, c)$, where $c \in \{R, G, B\}$. However, because reflectance characteristics are wavelength-dependent, RGB BTFs are insufficient for accurate reproduction of material appearance under various lighting conditions. Hence, in practical applications, the efficient acquisition of spectral BTFs becomes an issue that must be resolved.

In this paper, we propose a framework for efficient spectral BTF acquisition and reconstruction. As illustrated in Fig. 2, the framework comprises an imaging stage and a spectral BTF reconstruction stage. In the imaging stage, the RGB BTF data is acquired by a BTF imaging system equipped with color cameras. Besides, one spectral image is captured under a specific viewing direction using a multispectral imaging system. In this way, the total measurement time is almost identical to that of the RGB BTF imaging system. In the reconstruction stage, spectral BTFs are obtained by fusing the RGB and spectral images. This is achieved by reconstructing spectral reflectance from RGB values using nonnegative matrix factorization (NMF). In the experiments, we evaluate the accuracy of spectral reconstruction on both synthetic and real data, and also illustrate the appearances of spectral BTFs under various illumination conditions.

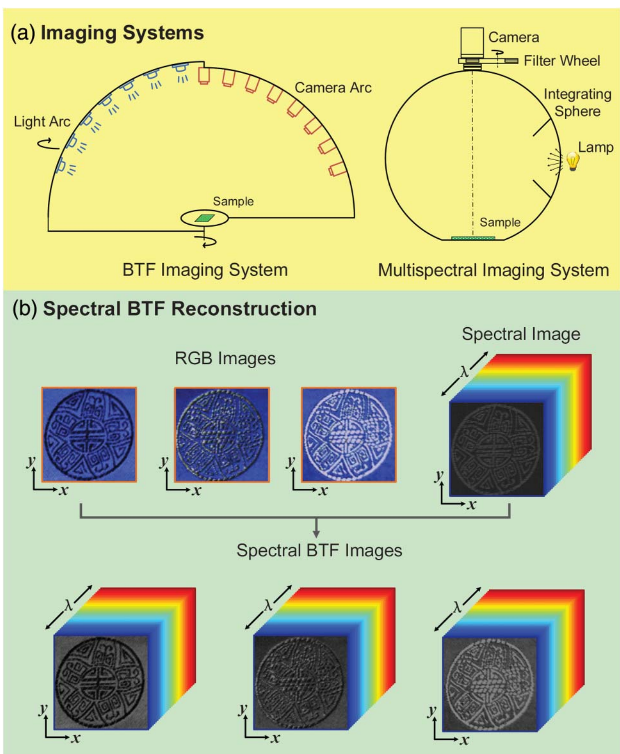

Fig. 2. Proposed framework for spectral BTF acquisition and reconstruction.

A. Background and Related Work

A classical measurement device for BRDF acquisition is the gonioreflectometer, which mechanically moves the light source and the detector from one position to another around the sample [1]. The work [5] developed an image-based rapid acquisition system, which can efficiently capture isotropic BRDFs by using the spherically homogenous samples of the materials. The Mitsubishi Electric Research Laboratories (MERL) database, which was collected in [5], contains the dense-sampled isotropic BRDF data of 100 real materials, including fabrics, painted surfaces, plastics, metals, etc. In [12], a robot-based gonioreflectometer was used to capture spectral BRDFs with a spectroradiometer as the measurement device. An image-based gonio-spectrophotometer system was introduced in [13] to acquire the spectral BRDF of pearlescent paints by combining high dynamic range (HDR) images and multispectral images.

The BTF measurement device is usually equipped with a camera and a light source. Typically, the camera and the light source move over a hemisphere above the planar material sample [6,11,14]. The measurement process for a material can take dozens of hours when measuring a material. To reduce measurement time, the work [15] used an array of 151 commodity digital still cameras mounted on a hemispherical gantry for BTF collection. With the expensive hardware, the system was capable of taking 22801 (151×151) images in less than an hour. Liu *et al.* [16] built a dome with LEDs of different colors to acquire spectral BTF. They learned discriminative illumination patterns from spectral BTFs to classify materials but did not measure the entire spectral BTF data. To the best of our knowledge, only [17] proposed a method for entire spectral BTF acquisition. In [17], the multispectral imaging device consisted of a camera and a liquid-crystal tunable filter. The spectral BTFs were acquired by sequentially rotating the imaging device and sample table. However, the system needs more than three days to measure a material, much longer than traditional RGB BTF imaging systems. Hence this system is not suitable for massive BTF collection.

As mentioned, our proposed spectral BTF acquisition framework is based on spectral reflectance reconstruction. In the color science literature, a number of spectral reflectance reconstruction algorithms have been proposed over the decades [18–26]. Among these, Wiener estimation (WE) is the widely adopted one [19–21]. The WE algorithm minimizes the mean squared error of the reconstructed reflectance, and the real one under certain assumptions about the signal and noise statistics [20]. In [21], an adaptive WE algorithm was introduced to improve the accuracy of spectral reflectance reconstruction by adaptive training sample selection and weighing.

In additional to WE, the techniques based on principal component analysis (PCA) [27] are also widely adopted for spectral reflectance reconstruction [22,23,28]. This is due to the fact that the spectral reflectances of natural and man-made surfaces are generally smooth, and thus can be represented by the linear combinations of basis functions [29]. The basis functions can be straightforwardly obtained using PCA. In [24], nonnegative principal component analysis (NNPCA) [30] was adopted in computing basis functions, to ensure that the reconstructed spectral reflectances are nonnegative. It was reported [24] that the reconstruction accuracy of the NNPCA algorithm is better than, or close to, the PCA algorithm.

B. Our Contributions

The contributions of this work are twofold. First, a framework is proposed for efficient spectral BTF acquisition and reconstruction with solid theoretical and practical analysis. Second, a new algorithm is introduced for spectral reflectance reconstruction by using NMF. The accuracy of spectral BTF reconstruction is validated by extensive experiments.

2. SPECTRAL BTF ACQUISITION AND RECONSTRUCTION

A. Analysis of Imaging Models

The two imaging systems used in this work are illustrated in Fig. 2(a). The BTF imaging system is a combination of gonioreflectometer structure and camera/light source arrays. It consists of eight RGB cameras and seven LED light sources, installed on two arcs with an interval step 10°. When capturing BTFs, the camera arc keeps fixed, while the light arc and sample table are sequentially rotated to predefined positions. The multispectral imaging system comprises a monochrome camera, a filter wheel, and an integrating sphere [31,32]. The sample is placed in the integrating sphere. Light rays are, by multiple scattering reflections inside the integrating sphere, uniformly distributed on the sample surface. The bandpass optical filters, which cover the visible spectrum from 400 to 700 nm, are mounted on a rotating wheel, and images are then sequentially captured by positioning the filters in front of the camera. With appropriate system calibration, the spectral reflectance of each pixel is computed from the multichannel camera responses [21,33]. The spectral accuracy of the acquired spectral image is close to a standard spectrophotometer, which also adopts an integrating sphere as its major optical component.

We first introduce the imaging model of the BTF system. Suppose that the response of the camera is proportional to the intensity of light entering the sensor, the camera response u_c, $c \in \{R, G, B\}$, can be formulated as

$$u_c(p, \omega_i, \omega_o) = \int s_c(\lambda) f(p, \omega_i, \omega_o, \lambda) l_{\mathrm{BTF}}(\omega_i, \lambda) \cos\theta_i \mathrm{d}\lambda, \tag{3}$$

where $s_c(\lambda)$ denotes the following: the spectral sensitivity function of the camera at channel c; $l_{\mathrm{BTF}}(\omega_i, \lambda)$, the spectral power distribution of the light source from direction ω_i; and θ_i, the angle between ω_i and surface normal. The light intensity from all the directions are the same after system calibration, so we have $l_{\mathrm{BTF}}(\omega_i, \lambda) = l_{\mathrm{BTF}}(\lambda)$. In practical computation, the continuous functions are replaced by their sampled counterparts, and the integral is written as summation. If $N(=31)$ uniformly spaced samples are used over the visible spectrum, Eq. (3) can be written in its vector and matrix notation as

$$\mathbf{u}(p, \omega_i, \omega_o) = \mathbf{M}\mathbf{f}(p, \omega_i, \omega_o) \cos\theta_i, \tag{4}$$

where $\mathbf{M} \in \mathbb{R}^{3\times N}$ represents the spectral responsivity incorporating the spectral power distribution of light source and spectral sensitivity function of camera, $\mathbf{f}(p, \omega_i, \omega_o) \in \mathbb{R}^{N\times 1}$ is the BTF vector, and $\mathbf{u}(p, \omega_i, \omega_o) \in \mathbb{R}^{3\times 1}$ is the camera response vector.

In the multispectral imaging system, the measured spectral reflectance $r(p, \lambda)$ can be represented as

$$r(p, \lambda) = \frac{\int_\Omega f(p, \omega_i, \widetilde{\omega}_o, \lambda) l_{\mathrm{MSI}}(\omega_i, \lambda) \cos\theta_i \mathrm{d}\omega_i}{\int_\Omega l_{\mathrm{MSI}}(\omega_i, \lambda) \cos\theta_i \mathrm{d}\omega_i}, \tag{5}$$

where $\widetilde{\omega}_o := (\widetilde{\theta}_o, \widetilde{\phi}_o) = (0°, 0°)$ is the direction of the camera, which is orthographic to the sample surface. The notation Ω represents the hemisphere range of lighting directions, and $l_{\mathrm{MSI}}(\omega_i, \lambda)$ denotes the spectral power distribution of light source at direction ω_i. In an integrating sphere the light intensities from all directions can be considered identical, hence Eq. (5) becomes

$$r(p, \lambda) = \frac{1}{4} \int_\Omega f(p, \omega_i, \widetilde{\omega}_o, \lambda) \cos\theta_i \mathrm{d}\omega_i. \tag{6}$$

The integrating sphere light can be regarded as a collection of numerous point light sources distributed over the hemisphere. Letting $\{\omega_i^1, \omega_i^2, \ldots, \omega_i^K\}$ be the K sampled lighting, Eq. (6) can be discretized as

$$r(p, \lambda) = \lim_{K\to\infty} \frac{\pi}{2K} \sum_{k=1}^{K} f(p, \omega_i^k, \widetilde{\omega}_o, \lambda) \cos\theta_i^k. \tag{7}$$

In the following we analyze the relationship between the RGB and multispectral imaging models by simulation. Suppose that a virtual RGB camera, which is of the same spectral sensitivity of that in the BTF system, replaces the multispectral camera in the multispectral imaging system. Denoting $\mathbf{r}(p) = (r(p, \lambda_1), \ldots, r(p, \lambda_N))^{\mathrm{T}}$ and supposing $l_{\mathrm{MSI}}(\omega_i, \lambda) = l_{\mathrm{BTF}}(\lambda)$, the response of the virtual RGB camera can be represented as

$$\mathbf{u}_{\mathrm{MSI}}^{\mathrm{virtual}}(p) = \mathbf{M}\mathbf{r}(p) = \lim_{K\to\infty} \frac{\pi}{2K} \sum_{k=1}^{K} \mathbf{M}\mathbf{f}(p, \omega_i^k, \widetilde{\omega}_o) \cos\theta_i^k. \tag{8}$$

Combining Eqs. (4) and Eq. (8) yields

$$\mathbf{u}_{\mathrm{MSI}}^{\mathrm{virtual}}(p) = \lim_{K\to\infty} \frac{\pi}{2K} \sum_{k=1}^{K} \mathbf{u}(p, \omega_i^k, \widetilde{\omega}_o) \approx \frac{\pi}{2} \bar{\mathbf{u}}_K(p), \tag{9}$$

where

$$\bar{\mathbf{u}}_K(p) = \frac{1}{K} \sum_{k=1}^{K} \mathbf{u}(p, \omega_i^k, \widetilde{\omega}_o) \tag{10}$$

is the mean image computed from the BTF images captured by the orthogonal (top view) camera under K lighting directions.

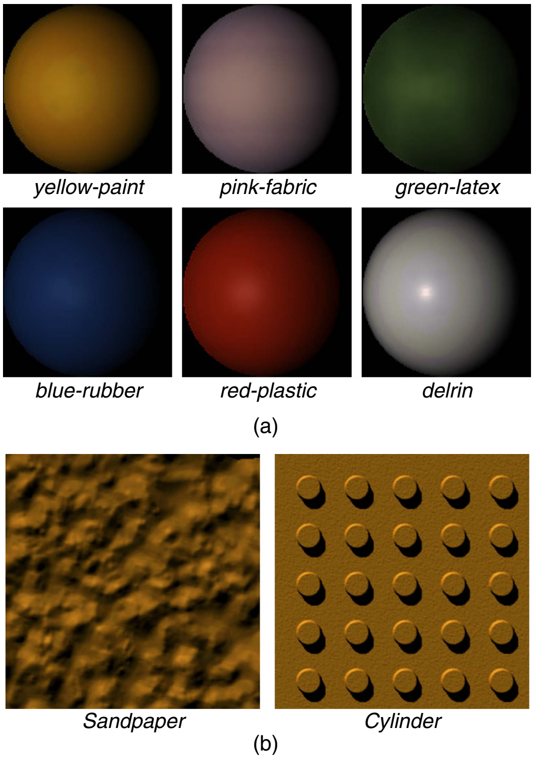

Fig. 3. Simulated BTF images of the 3D *Sandpaper* and *Cylinder* surfaces. (a) Six MERL BRDF materials. (b) Rendered surfaces using the MERL material yellow-paint.

We note that as the number of lighting directions, K, is limited in the BTF imaging system, the equality in expression (9) does not strictly hold. Nevertheless, our simulation on the MERL database [5] reveals that the approximation holds for real materials without strong specular reflections. As mentioned in Section 1, the MERL database contains densely sampled BRDF data. To validate our hypothesis on BTF images, we rendered two typical 3D surfaces using BRDF data and simulated shadow by ray tracing [34]. Other light-surface interaction phenomena such as interreflection are not considered as they are not quite influential to the analysis. Figure 3(a) shows 6 MERL BRDF materials used in our simulation. It is observed that materials *red-plastic* and *delrin* have some specular reflection, and the other four materials are mainly of diffuse reflection. For visualization purpose, Fig. 3(b) illustrates the two surfaces (*Sandpaper* and *Cylinder*) rendered using the material *yellow-paint* under specific lighting and viewing directions.

For quantitative analysis, Table 1 lists the average responses and relative errors of the mean BTF images of the two surfaces rendered with the six BRDF materials. The number of the lighting direction, K, is determined by the rotation intervals of light arc $\Delta\phi_i$. In the simulation we set the interval $\Delta\phi_i = 10°$, $20°$, or $30°$. It is seen that the relative errors of mean image approximation are less than 1.5% in all cases. This finding motivates us to reconstruct spectral BTFs using the computed mean BTF image $\bar{\mathbf{u}}(p)$ and the captured spectral image $\mathbf{r}(p)$.

B. Spectral BTF Reconstruction

The spectral reflectance reconstruction problem can be formulated to find a transform that converts the camera responses to spectral reflectance. In this paper, the RGB values of training color samples are from the mean RGB BTF image, and the spectral reflectance counterparts are from the captured spectral image.

In the following, we introduce our new spectral reconstruction algorithm, which is based on NMF [35]. NMF factorizes a nonnegative matrix, whose entries are either positive or zero, into two low-rank nonnegative matrices. The use of NMF is reasonable, because the spectral reflectances of object surfaces are physically nonnegative.

To simplify notations, the variable p (pixel position) will be omitted hereafter without causing confusion. Owing to the smooth property of spectral reflectance, $\mathbf{r}$ is represented by the linear combination of $J(< N)$ basis functions [29,28],

$$\mathbf{r} = \mathbf{B}\mathbf{a}, \tag{11}$$

where $\mathbf{B} \in \mathbb{R}^{N\times J}$ is the matrix of basis functions, and $\mathbf{a} \in \mathbb{R}^{J\times 1}$ is the corresponding coefficient vector. In this paper, we set $J = 3$ as only 3 channels are available in the mean BTF image. Then the imaging model can be written as

$$\mathbf{u} = \mathbf{M}\mathbf{r} = \mathbf{M}\mathbf{B}\mathbf{a} = \mathbf{G}\mathbf{a}, \tag{12}$$

where we denote $\mathbf{G} \coloneqq \mathbf{M}\mathbf{B}$. Note that here we have made the constant scale $\pi/2$ in expression (9) be subsumed into the spectral responsivity matrix $\mathbf{M}$.

Table 1. Average Responses (Relative Error) of the Mean BTF Images, with The BTF Images Simulated from the *Sandpaper* and *Cylinder* Surfaces, and Rendered by Six MERL BRDF Materials[a]

	Yellow-Paint	Pink-Fabric	Green-Latex	Blue-Rubber	Red-Plastic	Delrin
Sandpaper						
Densely sampled	50.01	75.68	32.18	29.79	37.57	90.06
$\Delta\phi_i = 10°(K = 245)$	50.21 (0.40%)	75.51 (0.23%)	31.91 (0.85%)	29.77 (0.09%)	37.48 (0.24%)	89.80 (0.29%)
$\Delta\phi_i = 20°(K = 119)$	50.21 (0.40%)	75.51 (0.23%)	31.91 (0.85%)	29.77 (0.09%)	37.48 (0.24%)	89.80 (0.29%)
$\Delta\phi_i = 30°(K = 77)$	50.22 (0.43%)	75.51 (0.23%)	31.92 (0.83%)	29.78 (0.05%)	37.48 (0.24%)	89.80 (0.29%)
Cylinder						
Densely sampled	50.82	76.20	33.94	30.83	39.22	95.44
$\Delta\phi_i = 10°(K = 245)$	50.71 (0.23%)	75.93 (0.35%)	33.75 (0.57%)	30.54 (0.93%)	38.94 (0.71%)	94.05 (1.46%)
$\Delta\phi_i = 20°(K = 119)$	50.71 (0.23%)	75.93 (0.35%)	33.75 (0.57%)	30.54 (0.93%)	38.94 (0.71%)	94.05 (1.46%)
$\Delta\phi_i = 30°(K = 77)$	50.71 (0.23%)	75.97 (0.30%)	33.76 (0.54%)	30.55 (0.90%)	38.96 (0.67%)	94.01 (1.49%)

[a]The number of lighting directions, K, is determined by rotation interval $\Delta\phi_i$.

Denote P as the number of pixels in the mean BTF (or spectral) images. Further denote $\mathbf{R} \in \mathbb{R}^{N\times P}$ as the reflectance matrix that stacks all the reflectances in the spectral image, and $\mathbf{U} \in \mathbb{R}^{3\times P}$ the response matrix that stacks all the RGB values in the mean BTF image. According to Eqs. (11) and (12), we have $\mathbf{R} = \mathbf{BA}$ and $\mathbf{U} = \mathbf{GA}$, where $\mathbf{A} \in \mathbb{R}^{J\times P}$ is the coefficient matrix. Our aim is to find matrices $\mathbf{B}$, $\mathbf{G}$, and $\mathbf{A}$ that minimize the two representations. Since spectral reflectance and RGB values cannot be negative, it is natural to impose a nonnegative constraint on the basis function matrix and coefficient matrix. Hence, the objective function can be formulated as

$$\{\mathbf{B}, \mathbf{G}, \mathbf{A}\} = \arg\min_{\mathbf{B},\mathbf{G},\mathbf{A}} \|\mathbf{R} - \mathbf{BA}\|_F^2 + \gamma\|\mathbf{U} - \mathbf{GA}\|_F^2,$$
$$\text{s.t.} \quad \mathbf{B} \geq 0, \mathbf{G} \geq 0, \mathbf{A} \geq 0, \tag{13}$$

where the subscript F denotes the Frobenius norm, and the parameter γ balances the two error terms. Denoting $\mathbf{X} = (\mathbf{R}, \sqrt{\gamma}\mathbf{U})^{\mathrm{T}}$ and $\mathbf{D} = (\mathbf{B}, \sqrt{\gamma}\mathbf{G})^{\mathrm{T}}$, Eq. (13) can be transformed to the standard NMF formulation,

$$\{\mathbf{D}, \mathbf{A}\} = \arg\min_{\mathbf{D},\mathbf{A}} \|\mathbf{X} - \mathbf{DA}\|_{\mathrm{F}}^2, \quad \text{s.t.} \quad \mathbf{D} \geq 0, \mathbf{A} \geq 0, \tag{14}$$

which can be solved using the NMF solver in [36]. In this paper, we simply set $\gamma = 1$.

After obtaining the matrices $\mathbf{B}$ and $\mathbf{G}$, the spectral reflectance can be computed from RGB values. For a specific RGB response $\mathbf{u}_s$, its corresponding coefficient is computed by

$$\hat{\mathbf{a}} = \arg\min_{\mathbf{a}} \|\mathbf{u}_s - \mathbf{Ga}\|_2^2, \quad \text{s.t.} \quad \mathbf{a} \geq 0, \tag{15}$$

and the spectral reflectance is reconstructed as

$$\hat{\mathbf{r}}_s = \mathbf{B}\hat{\mathbf{a}}. \tag{16}$$

3. EXPERIMENTS

In the experiments, we evaluate the proposed spectral reconstruction algorithm on both synthetic and real data. The synthetic data are generated based on the Bonn University spectral BTF dataset [37] that was captured using the method presented in [17]. The real RGB BTF images and the spectral image were captured using the imaging systems shown in Fig. 2(a). The spectral reconstruction accuracy of the proposed algorithm is compared to three baseline algorithms, i.e., WE [19,20], PCA algorithm [23,25], and NNPCA algorithm [24].

A. Synthetic Data Results

The spectral BTFs of two materials, namely, *Red-fabric* and *Lego-brick*, are used in the synthetic data experiment. Each material has 6561 spectral BTF images, captured under 81 viewing directions and 81 lighting directions. The pixel spectra are smoothed to reduce the unrealistic spectral fluctuations caused by limited imaging condition [37]. The corresponding RGB BTF images are generated from the spectral ones according to Eq. (4), by using the spectral responsivity identical to our BTF imaging system. Gaussian noise with zero mean and standard deviation 0.02 (in the range [0,1]) is added to simulate the noise level of our real BTF imaging process.

The accuracy of spectral reconstruction is evaluated in terms of spectral root-mean-squares (rms) error and colorimetric error. The latter is computed using the CIEDE2000 color difference (ΔE_{00}) formula [38] under CIE standard illuminants D65, F2, and A. Tables 2 and 3, respectively, show the colorimetric and spectral errors of the four algorithms. The viewing direction $(\theta_i, \phi_i) = (0°, 0°)$ that corresponds to the top-view camera is for training, and the other three directions are for testing. It is seen that the reconstruction errors of the proposed algorithm are lower than those of the competitors on both materials.

Figure 4 shows the reconstruction results of the material *Red-fabric* under three different combinations of viewing and lighting directions. It is observed that the spectral reflectance reconstructed by the proposed algorithm is the closest to ground truths, when compared to the other three algorithms.

Figure 5 further shows the reconstructed reflectances of the specified positions on the *Lego-brick* surface. This surface has a large height variation and contains distinct colors. It is observed that for both diffuse pixel A and specular pixel B, the spectral reflectances reconstructed by the proposed method are very close to the ground truths. For pixel C, which is not invisible to the top camera due to surface height, the spectral reflectance reconstructed by the proposed algorithm is still satisfactory.

B. Real Data Results

Figure 6 shows the example RGB BTF images of 19 materials captured by our BTF and multispectral imaging systems. These

Table 2. Colorimetric Errors Produced by Spectral Reflectance Reconstruction Algorithms[a]

	ΔE_{00} (D65)				ΔE_{00} (F2)				ΔE_{00} (A)			
	WE	PCA	NNPCA	Proposed	WE	PCA	NNPCA	Proposed	WE	PCA	NNPCA	Proposed
Red-fabric												
(0°, 0°)	1.16	1.03	1.06	0.65	1.12	0.90	0.91	0.69	1.21	1.06	1.07	0.62
(15°, 0°)	1.67	1.11	1.16	0.92	1.68	1.11	1.12	0.89	1.64	1.15	1.17	0.84
(45°, 120°)	1.93	1.26	1.31	1.03	1.97	1.27	1.29	0.98	1.79	1.23	1.26	0.90
(75°, 240°)	1.82	1.27	1.32	1.07	2.06	1.33	1.34	1.13	1.80	1.24	1.25	0.91
Lego-brick												
(0°, 0°)	1.09	1.02	1.02	0.94	1.15	1.12	1.12	0.99	1.00	1.12	1.12	0.97
(15°, 0°)	1.54	1.35	1.35	1.23	1.56	1.41	1.41	1.20	1.47	1.43	1.43	1.17
(45°, 120°)	1.49	1.33	1.33	1.21	1.50	1.39	1.39	1.19	1.41	1.41	1.41	1.16
(75°, 240°)	1.49	1.34	1.34	1.23	1.48	1.40	1.40	1.20	1.35	1.40	1.40	1.16

[a]The viewing direction $(\theta_o, \phi_o) = (0°, 0°)$ is for training, and the other three directions are for testing.

Table 3. Spectral RMS Errors Produced by the Spectral Reflectance Reconstruction Algorithms[a]

	Spectral RMS			
	WE	PCA	NNPCA	Proposed
Red-fabric				
(0°, 0°)	0.0025	0.0023	0.0024	0.0018
(15°, 0°)	0.0036	0.0042	0.0045	0.0032
(45°, 120°)	0.0042	0.0050	0.0054	0.0038
(75°, 240°)	0.0070	0.0074	0.0079	0.0065
Lego-brick				
(0°, 0°)	0.0059	0.0062	0.0062	0.0054
(15°, 0°)	0.0060	0.0059	0.0059	0.0056
(45°, 120°)	0.0069	0.0066	0.0066	0.0062
(75°, 240°)	0.0086	0.0082	0.0082	0.0079

[a]The viewing direction $(\theta_i, \phi_i) = (0°, 0°)$ is for training, and the other three directions are for testing.

materials belong to 5 categories (knitted fabric, yarn-dyed fabric, wallpaper, woven, and wood) and are of various color patterns. In the RGB BTF imaging system, the rotation intervals of the light arc and sample table are set as $\Delta\phi_i = 30°$. As only the top-view spectral BTFs are available (captured by the multispectral imaging system), in this experiment half pixels are randomly selected for training and the rest are for testing. The colorimetric and spectral errors of the four algorithms are shown in Table 4. It is observed that the mean and maximum

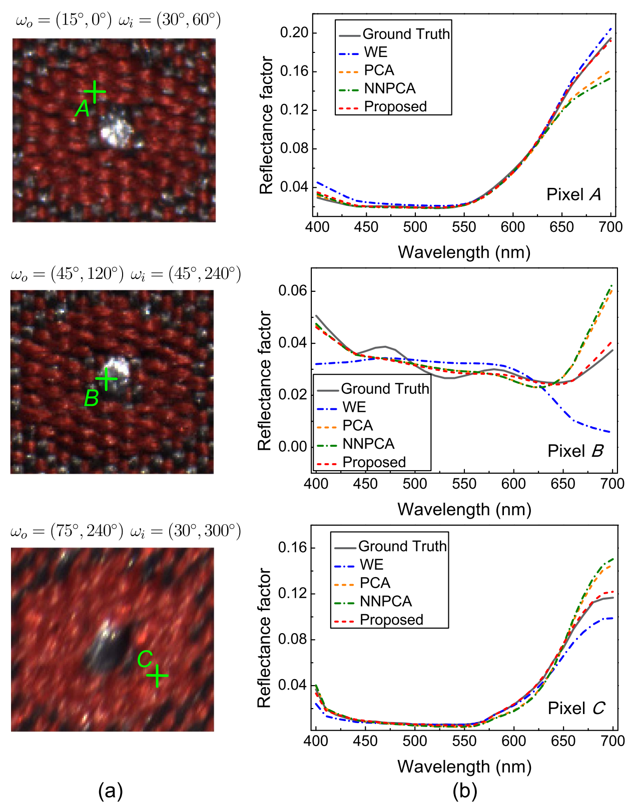

Fig. 4. Spectral reflectances reconstructed by different algorithms. (a) Images of the *Red-fabric* material under different lighting and viewing directions. (b) Reconstructed spectral reflectances of the specified pixels.

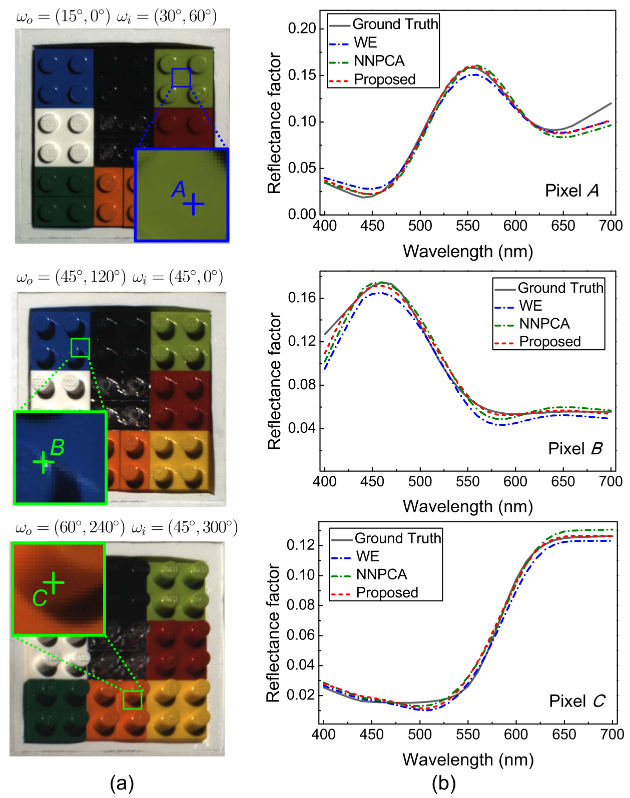

Fig. 5. Spectral reflectances reconstructed by different algorithms. Pixels *A* and *B* are of diffuse and specular reflections, respectively. Pixel *C* is not visible to the top camera due to surface height variation. (a) Images of the *Lego-brick* surface. (b) Reconstructed spectral reflectances of the specified pixels.

errors of the proposed algorithm are much lower than those of the three competitors.

Figure 7 shows the reconstructed spectral reflectances of the highlighted pixels in two BTF images. Note that the reflectances produced by the PCA algorithm are quite similar to those by the NNPCA algorithm, and hence are not shown for clear

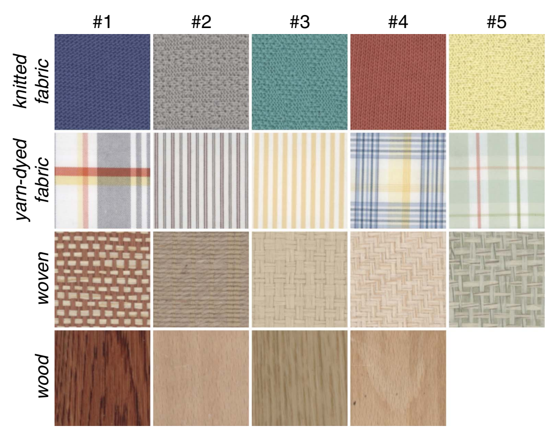

Fig. 6. Example images of the 19 real materials used in the experiment. Row 1: knitted fabric. Row 2: yarn-dyed fabric. Row 3: woven. Row 4: wood.

Table 4. Colorimetric and Spectral Errors (Mean and Maximum) Produced by Spectral Reflectance Reconstruction Algorithms on 19 Real Materials

	ΔE_{00} (D65)		ΔE_{00} (F2)		ΔE_{00} (A)		Spectral RMS	
	Mean	Max.	Mean	Max.	Mean	Max.	Mean	Max.
WE	1.33	3.15	1.29	2.80	1.33	4.02	0.017	0.049
PCA	3.10	5.89	3.39	7.82	2.95	5.62	0.071	0.255
NNPCA	2.94	5.62	2.92	7.84	1.81	3.26	0.067	0.209
Proposed	0.95	1.82	0.96	1.81	0.95	1.81	0.013	0.032

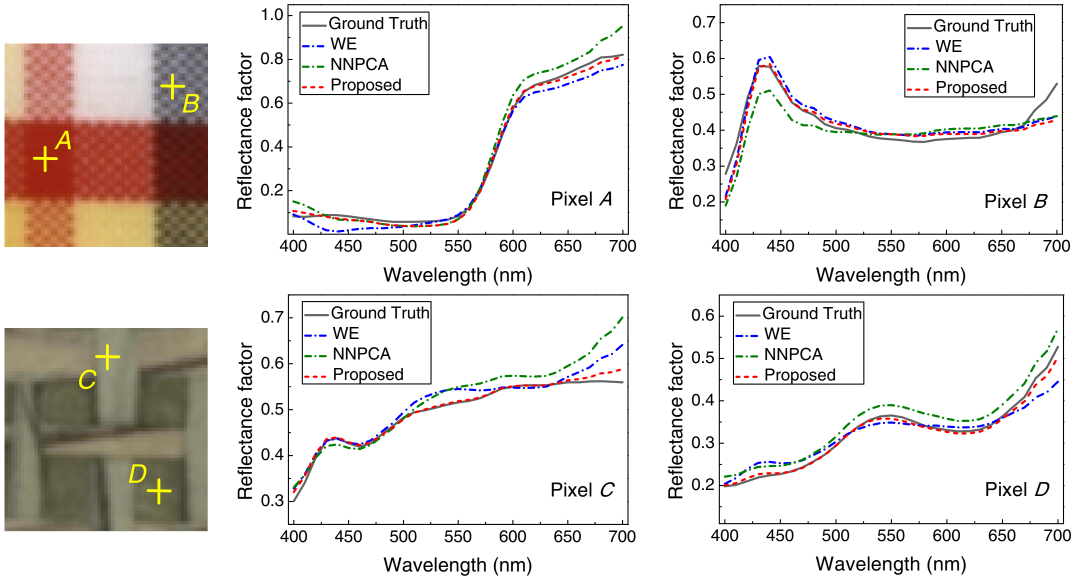

(a) (b)

Fig. 7. Spectral reflectances reconstructed by different algorithms. (a) Images of yarn-dyed fabric #1 and woven #5 materials. (b) Reconstructed spectral reflectances of the specified pixels.

visualization purpose. It is seen that the reflectance curves reconstructed by the proposed method are closer to ground truths, when compared to those by the WE and NNPCA algorithms.

C. Three-Dimensional Model Rendering

A conventional application of the spectral BTF is in rendering three-dimensional (3D) models under different illumination environments. In this spectral rendering procedure, the colorimetric CIEXYZ BTFs are computed from the reconstructed spectral BTFs and the spectral power distribution (SPD) of the CIE standard illuminants. The CIEXYZ BTFs are then converted to sRGB color space [39] for display. Figure 8 shows the 3D models (Sphere, Bunny, Cloth) rendered by three materials (knitted fabric #3, wood #1, and yarn-dyed fabric #4). The material *wood* #1 contains a few specular reflections, and the other two materials are of diffuse reflection. In Fig. 8, the first row shows the rendered results of the raw captured RGB BTFs, and the other rows demonstrate the rendered results of the reconstructed spectral BTF under three CIE standard illuminants. The visual appearances of the rendered 3D models can be very different under these illuminants. Overall, the rendered scenes appear quite natural for both diffuse and specular materials by using the spectral BTFs.

Colorimetric rendering can be a possible alternative to spectral rendering. In colorimetric rendering, the CIEXYZ BTFs under each illuminant are directly estimated from the acquired RGB BTFs, without using spectral reflectances. The transform between the acquired RGB values and CIEXYZ values can be modeled by two-order polynomial fitting [40]. However, due to the fitting error, the scenes produced by spectral rendering and colorimetric rendering are different. This is validated in Fig. 9. As shown, the color difference between the rendered scenes are visually obvious. Hence, spectral rendering should be used to achieve high color fidelity.

D. Efficiency

Our BTF imaging system acquires 7392 RGB images (96 views × 77 lights) for each material when setting the rotation intervals of the light arc and sample table as $\Delta\phi_i = 30°$. As shown in Table 5, the traditional full measurement technique needs 61.6 hours to capture all the 7392 multispectral images. In contrast, the proposed method costs 5.25 hours in capturing the RGB BTFs and 0.83 hours in reconstructing the

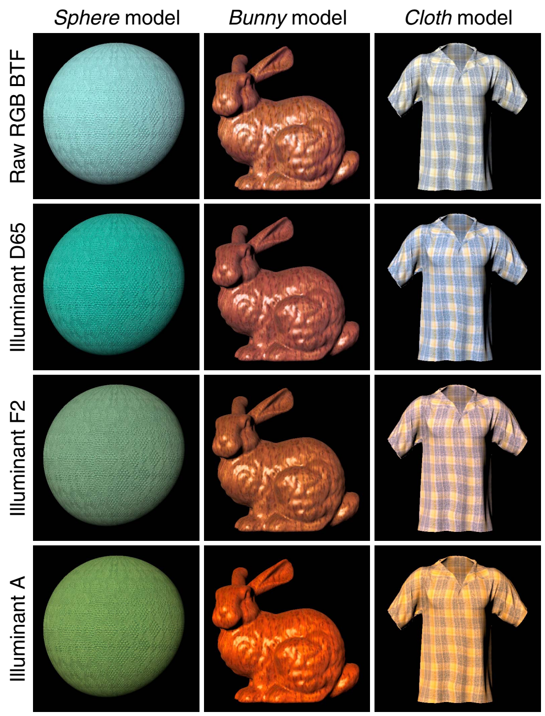

Fig. 8. Rendered 3D models. Row 1: rendered models using the captured (raw) RGB BTFs. Rows 2–4: rendered models using the reconstructed spectral BTFs (visualized under different illuminants).

spectral BTFs. In total, the proposed method obtains 9 × efficiency improvement compared to the full measurement technique.

The efficiency can be further improved in real applications. For example, in scene rendering it is not necessary to transform the acquired RGB BTFs to the spectral ones in advance. Actually, one can first render the 3D model with the raw RGB

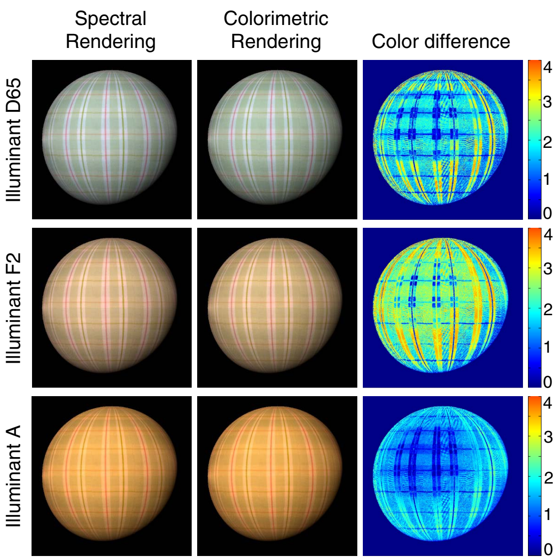

Fig. 9. Sphere model rendered by the spectral and colorimetric rendering techniques. The color difference maps (units: ΔE_{00}) are computed from the rendered scene pairs under individual illuminants.

Table 5. Time (Unit: Hours) Required for Spectral BTF Acquisition when Using the Traditional Full Measurement Technique and the Proposed Method

	Full Measurement	Proposed Method
Capturing	61.6	5.25
Reconstruction	–	0.83
Total	61.6	6.08

BTFs and then convert the rendered RGB scene to the spectral scene. In this way, much computational time and memory space can be saved.

4. CONCLUSIONS

This paper proposes a framework for efficient BTF acquisition and reconstruction. The framework acquires multiple RGB BTF images as usual and one additional spectral image. In this manner, the efficiency of data acquisition is totally determined by the RGB BTF imaging system. By exploring the relationship between the mean BTF images and the spectral image, spectral BTFs are reconstructed via image fusion. The spectral reflectance reconstruction is based on the linear representation of reflectance and NMF. It is verified that the proposed NMF-based algorithm outperforms the traditional ones on both synthetic and real data. The proposed framework is of practical application in reproducing visual appearances under different illumination conditions.

In this work an integrating sphere is used to produce uniform lighting in the multispectral imaging system. With this geometry, the spectral accuracy of the system is close to standard spectrophotometers. A limitation is that the proposed method will be not applicable to materials with strong specular highlight due to the geometrical inconsistency between the BTF and multispectral imaging systems. The exploration of both geometry compatibility and high spectral accuracy will be our future work on spectral BTF acqusition.

Funding. National Natural Science Foundation of China (NSFC) (61271339, 61371160); Hong Kong Research Institute of Textiles and Apparel (ITP/048/13TP).

REFERENCES

1. F. E. Nicodemus, J. C. Richmond, J. J. Hsia, I. W. Ginsberg, and T. Limperis, *Geometrical Considerations and Nomenclature for Reflectance* (U.S. Department of Commerce, National Bureau of Standards, 1977), Vol. **160**.
2. R. L. Cook and K. E. Torrance, “A reflectance model for computer graphics,” ACM Trans. Graph. **1**, 7–24 (1982).
3. G. J. Ward, “Measuring and modeling anisotropic reflection,” ACM SIGGRAPH Comput. Graph. **26**, 265–272 (1992).
4. X. D. He, K. E. Torrance, F. X. Sillion, and D. P. Greenberg, “A comprehensive physical model for light reflection,” ACM SIGGRAPH Comput. Graph. **25**, 175–186 (1991).
5. W. Matusik, H. Pfister, M. Brand, and L. McMillan, “A data-driven reflectance model,” ACM Trans. Graph. **22**, 759–769 (2003).
6. K. J. Dana, B. Van Ginneken, S. K. Nayar, and J. J. Koenderink, “Reflectance and texture of real-world surfaces,” ACM Trans. Graph. **18**, 1–34 (1999).

7. G. Müller, J. Meseth, and R. Klein, "Compression and real-time rendering of measured BTFs using local PCA," in *The 8th International Fall Workshop on Vision, Modeling and Visualisation* (2003), p. 271.
8. Y.-T. Tsai and Z.-C. Shih, "K-clustered tensor approximation: A sparse multilinear model for real-time rendering," ACM Trans. Graph. **31**, 1–17 (2012).
9. M. Sattler, R. Sarlette, and R. Klein, "Efficient and realistic visualization of cloth," in *Eurographics Symposium on Rendering* (2003), pp. 167–178.
10. J. Filip, R. Vávra, and M. Krupička, "Rapid material appearance acquisition using consumer hardware," Sensors **14**, 19785–19805 (2014).
11. G. Müller, J. Meseth, M. Sattler, R. Sarlette, and R. Klein, "Acquisition, synthesis, and rendering of bidirectional texture functions," Comput. Graph. Forum **24**, 83–109 (2005).
12. R. Baribeau, W. S. Neil, and E. Cote, "Development of a robot-based gonioreflectometer for spectral BRDF measurement," J. Mod. Opt. **56**, 1497–1503 (2009).
13. D. B. Kim, M. K. Seo, K. Y. Kim, and K. H. Lee, "Acquisition and representation of pearlescent paints using an image-based goniospectrophotometer," Proc. SPIE **49**, 043604 (2010).
14. M. L. Koudelka, S. Magda, P. N. Belhumeur, and D. J. Kriegman, "Acquisition, compression, and synthesis of bidirectional texture functions," in *3rd International Workshop on Texture Analysis and Synthesis* (2003), pp. 59–64.
15. G. Müller, G. H. Bendels, and R. Klein, "Rapid synchronous acquisition of geometry and appearance of cultural heritage artefacts," in *The 6th International Conference on Virtual Reality, Archaeology and Intelligent Cultural Heritage* (Eurographics Association, 2005), pp. 13–20.
16. C. Liu, G. Yang, and J. Gu, "Learning discriminative illumination and filters for raw material classification with optimal projections of bidirectional texture functions," in *IEEE Conference on Computer Vision and Pattern Recognition* (2013), pp. 1430–1437.
17. D. Lyssi, "A reflectometer setup for spectral BTF measurement," in *Spring Conference on Computer Graphics* (2009).
18. H. Haneishi, T. Hasegawa, A. Hosoi, Y. Yokoyama, N. Tsumura, and Y. Miyake, "System design for accurately estimating the spectral reflectance of art paintings," Appl. Opt. **39**, 6621–6632 (2000).
19. Y. Murakami, T. Obi, M. Yamaguchi, N. Ohyama, and Y. Komiya, "Spectral reflectance estimation from multi-band image using color chart," Opt. Commun. **188**, 47–54 (2001).
20. N. Shimano, "Recovery of spectral reflectances of objects being imaged without prior knowledge," IEEE Trans. Image Process. **15**, 1848–1856 (2006).
21. H.-L. Shen, P.-Q. Cai, S.-J. Shao, and J. H. Xin, "Reflectance reconstruction for multispectral imaging by adaptive Wiener estimation," Opt. Express **15**, 15545–15554 (2007).
22. D.-Y. Tzeng and R. S. Berns, "A review of principal component analysis and its applications to color technology," Color Res. Appl. **30**, 84–98 (2005).
23. F. Ayala, J. F. Echávarri, P. Renet, and A. I. Negueruela, "Use of three tristimulus values from surface reflectance spectra to calculate the principal components for reconstructing these spectra by using only three eigenvectors," J. Opt. Soc. Am. A **23**, 2020–2026 (2006).
24. M.-H. Lee, H. Park, I. Ryu, and J.-I. Park, "Fast model-based multispectral imaging using nonnegative principal component analysis," Opt. Lett. **37**, 1937–1939 (2012).
25. V. Cheung, C. Li, J. Hardeberg, D. Connah, and S. Westland, "Characterization of trichromatic color cameras by using a new multispectral imaging technique," J. Opt. Soc. Am. A **22**, 1231–1240 (2005).
26. H.-L. Shen and J. H. Xin, "Spectral characterization of a color scanner based on optimized adaptive estimation," J. Opt. Soc. Am. A **23**, 1566–1569 (2006).
27. I. Jolliffe, *Principal Component Analysis* (Wiley, 2014).
28. M. Shi and G. Healey, "Using reflectance models for color scanner calibration," J. Opt. Soc. Am. A **19**, 645–656 (2002).
29. L. T. Maloney, "Evaluation of linear models of surface spectral reflectance with small numbers of parameters," J. Opt. Soc. Am. A **3**, 1673–1683 (1986).
30. R. Zass and A. Shashua, "Nonnegative sparse PCA," in *Neural Information Processing Systems* (2007), pp. 1561–1568.
31. H.-L. Shen, Z.-H. Zheng, W. Wang, X. Du, S.-J. Shao, and J. H. Xin, "Autofocus for multispectral camera using focus symmetry," Appl. Opt. **51**, 2616–2623 (2012).
32. S.-J. Chen and H.-L. Shen, "Multispectral image out-of-focus deblurring using interchannel correlation," IEEE Trans. Image Process. **24**, 4433–4445 (2015).
33. H.-L. Shen, J. H. Xin, and S.-J. Shao, "Improved reflectance reconstruction for multispectral imaging by combining different techniques," Opt. Express **15**, 5531–5536 (2007).
34. G. V. D. Bergen, "Efficient collision detection of complex deformable models using AABB trees," J. Graph. Tools **2**, 1–13 (1997).
35. D. D. Lee and H. S. Seung, "Learning the parts of objects by non-negative matrix factorization," Nature **401**, 788–791 (1999).
36. H. Kim and H. Park, "Nonnegative matrix factorization based on alternating nonnegativity constrained least squares and active set method," SIAM J. Matrix Anal. Appl. **30**, 713–730 (2008).
37. M. Rump, R. Sarlette, and R. Klein, "Groundtruth data for multispectral bidirectional texture functions," in *European Conference on Colour in Graphics, Imaging, and Vision* (2010), pp. 326–330.
38. M. R. Luo, G. Cui, and B. Rigg, "The development of the CIE 2000 colour-difference formula: CIEDE2000," Color Res. Appl. **26**, 340–350 (2001).
39. M. Anderson, R. Motta, S. Chandrasekar, and M. Stokes, "Proposal for a standard default color space for the internet-sRGB," in *4th Color and Imaging Conference* (Society for Imaging Science and Technology, 1996), pp. 238–245.
40. G. Hong, M. R. Luo, and P. A. Rhodes, "A study of digital camera colorimetric characterization based on polynomial modeling," Color Res. Appl. **26**, 76–84 (2001).